RSC Advances

PAPER

View Article Online
View Journal | View Issue



Cite this: *RSC Adv.*, 2021, **11**, 14814

# Novel poly(arylene ether ketone)/poly(ethylene glycol)-grafted poly(arylene ether ketone) composite microporous polymer electrolyte for electrical double-layer capacitors with efficient ionic transport†

Fangyuan Hu, *[a] Yiting Liu,[a] Wenlong Shao,[b] Tianpeng Zhang,[a] Siyang Liu,[a] Dongming Liu,[a] Shouhai Zhang [b] and Xigao Jian [ab]

Polymer electrolytes have attracted considerable research interest due to their advantages of shape control, excellent safety, and flexibility. However, the limited use of traditional polymer electrolytes in electric double-layer capacitors due to their unsatisfactory ionic conductivities and poor mechanical properties makes them difficult to operate for long periods of time in large-scale energy storage. Therefore, we fabricated a high-performance microporous electrolyte based on poly(arylene ether ketone) (PAEK)/poly(ethylene glycol)-grafted poly(arylene ether ketone) (PAEK-*g*-PEG) using a certain amount of carboxylated chitosan with a high electrolyte uptake rate of 322 wt% and a high ionic conductivity of $2 \times 10^{-2}$ S cm$^{-1}$ at room temperature. A symmetric solid-state supercapacitor that uses activated carbon as electrodes and a composite microporous polymer film as the electrolyte shows a high specific capacitance of 134.38 F g$^{-1}$ at a current density of 0.2 A g$^{-1}$, while liquid electrolytes demonstrate a specific capacitance of 126.92 F g$^{-1}$. Energy density of the solid-state supercapacitor was 15.82% higher than that of the liquid supercapacitor at a current density of 5 A g$^{-1}$. In addition, the solid-state supercapacitor exhibited excellent cycling stability of over 5000 charge/discharge cycles at a current density of 1 A g$^{-1}$. Furthermore, solid-state supercapacitors display lower self-discharge behavior with an open-circuit potential drop of only 36% within 70 000 s, which is significantly better than that of conventional supercapacitors (52% @ 70 000 s), at a charging current density of 1 mA cm$^{-2}$. The satisfactory results indicated that the PAEK/PAEK-*g*-PEG composite microporous polymer film demonstrates high potential as an electrolyte material in practical applications of solid-state and portable energy storage devices.

Received 8th February 2021
Accepted 24th March 2021

DOI: 10.1039/d1ra01047f

rsc.li/rsc-advances



## 1. Introduction

Renewable energy storage and conversion systems have attracted considerable research attention due to the irreversible consumption of fossil fuels and growing energy demand.[1,2] Among various electrochemical energy storage systems, electric double-layer capacitors (EDLCs) are effective renewable energy storage systems and promising devices because of their high power density, satisfactory cyclic life, and rapid charge/discharge rate.[3,4] These advantages of EDLCs satisfy the requirement of portable electronic devices, energy-efficient industrial equipment, and hybrid electric vehicles.[5,6]

The performance of EDLCs mainly depends on the electrode material and electrolyte used.[7–9] Many electrode materials have been developed to improve the performance of EDLCs (*e.g.*, energy density and specific capacitance).[10,11] Apart from electrodes, electrolytes are also a crucial component that significantly affects specific energy, lifespan, operating voltage, and safety properties of EDLCs.[12] Traditional liquid electrolytes are widely used despite their limitations, such as their susceptibility to leakage during usage and nonflexibility.[13–15] Furthermore, flammable organic liquid electrolytes can result in the risk of combustion. These factors have impeded the practical application of EDLCs in large-scale energy storage systems.[13] Solid electrolytes were developed to overcome the shortcomings of their liquid counterpart. Meanwhile, polymer electrolytes have attracted considerable research attention due to their

[a]*School of Materials Science and Engineering, State Key Laboratory of Fine Chemicals, Key Laboratory of Energy Materials and Devices (Liaoning Province), Liaoning Province Engineering Centre of High Performance Resins, Dalian University of Technology, Dalian, 116024, China. E-mail: hufangyuan@dlut.edu.cn*

[b]*State Key Laboratory of Fine Chemicals, Liaoning Province Engineering Research Centre of High Performance Resins, Dalian University of Technology, Dalian, 116024, China*

† Electronic supplementary information (ESI) available. See DOI: 10.1039/d1ra01047f

excellent safety and flexibility. The three types of polymer electrolytes include solid (SPEs),[16] gel (GPEs), and microporous (MPEs) polymer electrolytes.[17,18] Ion conductivity of SPEs is excessively low at room temperature despite their satisfactory mechanical properties. The ionic conductivity of GPEs at room temperature is similar to that of liquid electrolyte, but their excessively poor mechanical properties make them unsuitable for large-scale energy storage.[18] An ideal solid electrolyte should exhibit excellent ionic conductivity at room temperature and sufficient mechanical strength.[19] MPEs with these features are considered promising electrolytes because of their micropores, polymer membrane matrix, and ability to retain a large amount of electrolytes in the pore structure to ensure ionic conductivity.[12] Nonsolvent-induced phase separation (NIPS), a conventional method for fabricating MPEs, has been used to create ion transport channels.[20] The hydrophilic segment of copolymer moves to the isopropanol-rich phase and remains on the pore surface of the obtained porous membrane when a copolymer is used to prepare porous membranes in the NIPS process with isopropanol as the coagulation bath. This method has been widely used in the fabrication of functional porous polymer membranes.[21] Moreover, the ionic conductivity mainly depends on the absorption of MPEs by micropores. The morphology of MPEs, including porosity, pore size, and pore distribution, remarkably affects the absorption of electrolytes and thus seriously influences the ionic conductivity of MPEs.[22,23]

Many polymers, such as polyvinyl alcohol (PVA),[24] poly(ethylene oxide) (PEO),[25] polyacrylonitrile (PAN),[26] poly(vinylidene fluoride) (PVDF),[27] poly(vinylidene fluoride-*co*-hexafluoropropylene) (PVDF-HFP),[28] and their blends, are used in MPEs. PEO-based polymers are widely applied in electrolytes due to their unique structure, which can form complexes with lithium salt.[29,30] Poly(ethylene glycol) (PEG) was selected as the hydrophilic segment in the preparation of porous membranes in previous studies.[31] In summary, these advantages of PEO-based polymers can lead to high ionic conductivity.[32] However, excessively poor mechanical properties of PEO-based polymers make them unsuitable for the application of MPEs.[12] Therefore, developing new material for MPEs with mechanical properties and high solvation efficiency with lithium salts is critical. Poly(arylene ether ketone) (PAEK) polymers are a thermoplastic material with excellent thermal and mechanical properties widely applied in fuel cells.[33–35] However, the immiscibility of PAEK and PEG can lead to large-scale phase separation. Na *et al.*[12] prepared PAEK/PAEK-*g*-PEG composite MPEs that demonstrate high ionic conductivity of $8 \times 10^{-3}$ S $cm^{-1}$ at room temperature *via* grafting method to increase their compatibility. However, synthesized polymers contain a certain amount of fluorine, which can cause air pollution by releasing fluorine-containing gases in the event of dangerous combustion, and the low porosity caused by the nonideal porous structure of the membrane limits the further improvement of ion conductivity. We molecularly designed and developed high-performance PAEK material with satisfactory mechanical properties and excellent thermal stability. The results of our previous studies indicated that the use of total aryl, twisted and noncoplanar 4-(4-hydroxyl-phenyl)(2H)-phthalazine-1-one (DHPZ) effectively increases thermal properties and solubility of PAEK.[36–39] Therefore, PAEK was synthesized *via* aromatic nucleophilic substitution reaction and PAEK-*g*-PEG was synthesized using PAEK with free carboxyl groups and asymmetric methoxypolyethylene glycol to introduce PEG pendant groups through catalyzed esterification reactions of *N*,*N*′-dicyclohexylcarbodiimide (DCC) and 4-(dimethylamino) pyridine (DMAP). The PAEK main-chain backbone of PAEK-*g*-PEG shows excellent compatibility with PAEK, while PEG pendant groups show affinity with nonsolvent isopropanol through a hydrogen bond that results in enhanced pore structures. In addition, the formation of complexes of EO units in PAEK-*g*-PEG with lithium ion is beneficial to the transport of lithium ions and further improvement of the ionic conductivity.[40,41]

This study aimed to fabricate a high-performance MPE with excellent thermal stability and high ionic conductivity for EDLCs. We mixed PAEK-*g*-PEG with PAEK as the MPE matrix. The porosity, pore distribution, and diameter of MPEs can be controlled by adjusting the content of PAEK-*g*-PEG segments. Suitability of MPEs with high porosity and acceptable mechanical properties was determined by adjusting the ratio of the two components. The aqueous $LiClO_4$ solid electrolyte was obtained by adding the appropriate amount of chitosan to improve the liquid-retention capacity of electrolytes. The PAEK/PAEK-*g*-PEG composite membrane was then soaked in the aqueous $LiClO_4$ electrolyte with chitosan to form MPEs. Solid-state EDLCs with activated carbon as the electrode were prepared using the obtained MPEs. The electrochemical performance of EDLC with MPEs and commercial separators were investigated *via* cyclic voltammetry (CV), galvanostatic charge/discharge (GCD) measurements, electrochemical impedance spectroscopy (EIS), and self-discharge tests.

## 2. Experimental

### 2.1 Material synthesis

**Chemical and materials.** All starting materials used are commercially available and used without further purification unless otherwise indicated. Anhydrous THF was refluxed and distilled from sodium and benzophenone.

**Synthesis of PAEK, PAEK with carboxyl pendant (PAEK–COOH), and PAEK-*g*-PEG.** PAEK was synthesized using the aromatic nucleophilic substitution reaction method applied in previous studies.[42,43] PAEK was synthesized using 4,4′-difluorobenzophenone (DFBP), 4-(4-hydroxyl-phenyl)(2H)-phthalazine-1-one (DHPZ) as illustrated in Scheme 1. The synthetic procedure (PAEK) was carried out as follows: DFBP (5.2390 g, 24.01 mmol), DHPZ (5.7178 g, 24 mmol), toluene (10 ml), and anhydrous $K_2CO_3$ (4.64 g, 33.6 mmol) were dissolved in TMS (10 ml) in a three-necked flask equipped with a mechanical stirrer, a nitrogen inlet, and a Dean–Stark trap with a condenser. The mixture was refluxed for 2 h at 150 °C under nitrogen to remove the resulting water. Toluene was then removed at 160 °C. The mixture reaction was continued for 8 h at 190 °C to complete polymerization. TMS (20 ml) was added and stirred for 20 minutes after polymerization. The viscous solution was

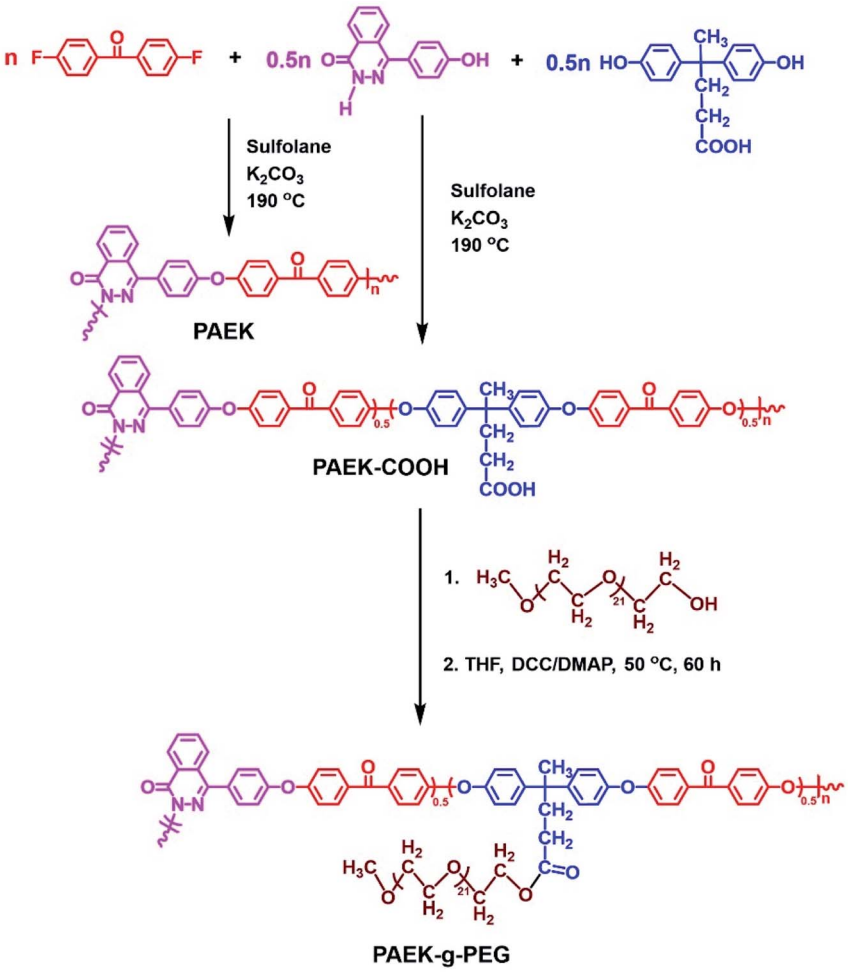


Scheme 1 Synthesis of PAEK, PAEK–COOH, and PAEK-*g*-PEG copolymers.

subsequently poured into boiling water to precipitate the polymer. Boiled the product in deionized water five times and then dried it. Yield: 91%. $M_n$: 61.6 kg mol$^{-1}$. IR (Fig. S2†): $\nu_{max}$ (cm$^{-1}$): 1661 (Ar–C=O), 1591, 1504 (Ar), 1237 (Ar–O–Ar).

PAEK–COOK was prepared using a similar synthesis procedure to that of PAEK. Then, 10 g of PAEK–COOK was dissolved in 200 ml of THF and 20 ml of concentrated HCl was added in a drop-wise manner while stirring. The mixture was continuously stirred for 8 h to ensure that the reaction was completed. Third, the product was poured in deionized water and dried to constant weight. Yield (82%). $M_n$: 24.4 kg mol$^{-1}$. IR (Fig. S2†): $\nu_{max}$ (cm$^{-1}$): 1730 (O=C–OH), 1591, 1504 (Ar), 1237 (Ar–O–Ar), 1661 (Ar–C=O).

The synthesis procedure of the PAEK-*g*-PEG polymer was conducted as follows: 10 g of PAEK–COOH, 30 g (30 mmol) of MPEG (methoxypolyethylene glycol, $M_n$ = 1000 g mol$^{-1}$), 100 ml of anhydrous THF were added to a three-necked flask equipped with a mechanical stirrer and nitrogen inlet in nitrogen atmosphere. The mixture was continuously stirred until it was dissolved. An anhydrous THF solution (30 ml) made of 2.536 g (12.3 mmol) of DCC and 0.150 g (1.23 mmol) of DMAP was added in a drop-wise manner in 2 h to avoid the formation of gel. The reaction was continued at 50 °C for 60 h under nitrogen. The solution was filtered to remove the precipitate (dicyclohexylurea, DCU) and then precipitated in deionized water. The product was boiled thrice to remove the unreacted MPEG and then dried in a vacuum at 80 °C for 48 h. Yield: 78%. $M_n$: 33.9 kg mol$^{-1}$. IR (Fig. S2†): $\nu_{max}$ (cm$^{-1}$): 1730 (O=C–O–R), 1661 (Ar–C=O), 1591, 1504 (Ar), 1103 (–C–O–C–), 1237 (Ar–O–Ar), 2928 (–$CH_2$).

### 2.2 Preparation of PAEK/PAEK-*g*-PEG composite microporous polymer electrolyte

Microporous PAEK/PAEK-*g*-PEG composite membranes were fabricated *via* the NIPS process using 1-methyl-2-pyrrolidone (NMP) as the solvent of PAEK/PAEK-*g*-PEG and isopropanol as the coagulant (nonsolvent) (Scheme 2). PAEK and PAEK-*g*-PEG polymers were dissolved in NMP (solvent) and the mixture was stirred until a homogeneous solution formed. The viscous solution was then casted onto a clean glass plate at a temperature and humidity of 20 °C and 60%, respectively, for 3 minutes. The glass plate was then immersed in isopropanol for 30 minutes. Microporous membranes were prepared after drying to a constant weight in an oven at 80 °C for 24 h (as shown in

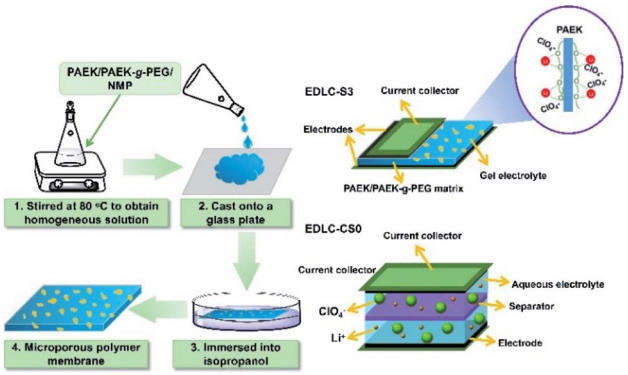


Scheme 2 Preparation of PAEK/PAEK-*g*-PEG composite microporous membranes and schematic diagram of the EDLC-S3 formed using S3 as the MPE and that of the EDLC-CS0 using CS0 as the separator.

Table 1 Labels and porosities of synthesized composite microporous membranes

| Label | PAEK/PAEK-*g*-PEG composition (wt/wt) | Porosity (%) |
|---|---|---|
| S0 | 10/0 | 39.4 |
| S1 | 9/1 | 67.8 |
| S2 | 8/2 | 77.0 |
| S3 | 7/3 | 84.2 |
| S4 | 6/4 | 72.5 |
| CS | NKK-MPF30AC-100[a] | 39.6 |

[a] NKK-MPF30AC-100 is commercial separator.

Fig. S3†). The weight ratio of the PAEK to PAEK-*g*-PEG in membranes was 10 : 0, 9 : 1, 8 : 2, 7 : 3, and 6 : 4 and then labeled S0, S1, S2, S3, and S4, respectively (Table 1).

A certain amount of carboxylated chitosan (mass fractions of carboxylated chitosan in $LiClO_4$ aqueous solution were 0, 1, 2, and 4 wt%) was added to the prepared 1 M $LiClO_4$ aqueous solution. The mixture was stirred continuously until the carboxylated chitosan dissolved completely. Microporous membranes were soaked in the $LiClO_4$ electrolyte solution for 1 h to prepare MPEs, which were then labeled C0, C1, C2, and C4. The commercial separator (NKK-MPF30AC-100) was also immersed in the 1 M $LiClO_4$ electrolyte without chitosan for comparison and then labeled CS0 (Table 2).

Table 2 Compositions of the various microporous polymer electrolytes

| Label | Membrane matrix | Carboxylated chitosan (wt%) |
|---|---|---|
| C0 | S3 | 0 |
| C1 | S3 | 1 |
| C2 | S3 | 2 |
| C4 | S3 | 4 |
| CS0 | NKK-MPF30AC-100 | 0 |

### 2.3 Characterization

**Material characterization.** $^1$H NMR and Fourier transform infrared (FT-IR) spectra of PAEK, PAEK–COOH, and PAEK-*g*-PEG were obtained with a Varian DLG400 using $CDCl_3$, DMSO and a Bruker Equinox 55 spectrometer, respectively. Molar masses were determined *via* gel permeation chromatography (GPC) with an Agilent 1260 infinity II high-temperature GPC system at 80 °C and run in NMP and calibrated against polystyrene standards. Thermal properties of MPEs were analyzed using thermogravimetric analysis (TGA). All membranes were fully dried under vacuum at 80 °C for 48 h before measurements. TGA was performed with a Mettler TGA/SDTA851 TGA thermal analyzer within 30–700 °C in nitrogen flow at a heating rate of 10 °C min$^{-1}$.

**Physical characterization of MPEs.** Morphologies of MPEs and the commercial separator (NKK-MPF30AC-100) were observed *via* scanning electron microscopy (SEM, HITACHI UHR FE-SEM SU8200).

The porosity ($P$%) of microporous membranes was calculated using the ethanol uptake test as follows:[17]

$$P\% = \frac{W - W_0}{\rho V} \times 100\%, \quad (1)$$

where $W$ and $W_0$ are weights of wet and dry microporous membranes, respectively; $\rho$ is the density of ethanol; and $V$ is the apparent volume of the porous membrane.

The electrolyte absorption ($W$%) and leakage capacity ($W_L$%) of membranes were determined as follows:[44]

$$W\% = \frac{M_{wet} - M_{dry}}{M_{dry}} \times 100\%, \quad (2)$$

$$W_L\% = \frac{M_{wet} - M_t}{M_{wet} - M_{dry}} \times 100\%, \quad (3)$$

where $M_t$ was measured after wiping with filter paper.

### 2.4 Electrode preparation, symmetric EDLC assembly, and electrochemical characterization of MPEs

EDLC was assembled by sandwiching MPEs between activated carbon electrodes to evaluate its electrochemical performance with MPEs (as shown in Fig. S5b, S6a and b†). Activated carbon cathode was prepared using a mixture of activated carbon, acetylene black, and PTFE at a weight ratio of 8 : 1 : 1.

The ionic conductivity of MPEs was measured *via* electrochemical impedance spectroscopy (EIS) measurements using a VMP3 electrochemical workstation with a voltage amplitude of 10 mV in the frequency range of 100 kHz to 1 Hz. Impedance spectra were obtained from 20 °C to 60 °C. The electrolyte membrane is sandwiched in two parallel stainless steel (as shown in Fig. S5a†). Ionic conductivity $\sigma$ was calculated as follows:[45]

$$\sigma = \frac{L}{R_b S} \quad (4)$$

where $L$ is the thickness and $S$ is the contact area between the electrolyte membrane and the stainless steel.

Cyclic voltammetry (CV), galvanostatic charging/discharging (GCD) and electrochemical impedance spectroscopy (EIS) tests of EDLC were performed using a VMP3 electrochemical workstation. The cyclic voltammetry (CV) was measured at different scan rates (5–200 mV $s^{-1}$) with a potential window of 0–1.5 V. The galvanostatic charge/discharge (GCD) test was recorded at various current densities (0.2, 0.5, 1, 2, and 5 A $g^{-1}$) in a potential range of 0–1.5 V. EIS measurements were carried out in a frequency range of 0.01 Hz to 100 kHz with a potential amplitude of 10 mV. The specific capacitance ($C_s$, F $g^{-1}$), energy density ($E_{cell}$, W h $kg^{-1}$), and power density ($P_{cell}$, W $kg^{-1}$) of the symmetrical electrode were calculated as follows:[46]

$$C_s = 4 \times \frac{I}{m(V/t)}, \quad (5)$$

$$E_{cell} = \left(\frac{C_s \times V^2}{8}\right) \times \frac{1000}{3600}, \quad (6)$$

$$P_{cell} = \frac{E_{cell}}{t} \times 1000, \quad (7)$$

where $I$ is the discharge current (A), $t$ is the discharge time (s), $m$ is the mass of the active material in the two electrodes (g), and $V$ is the potential window (V).

# 3. Results and discussion

## 3.1 Analysis of chemical structures of polymers

$^1$H NMR and FT-IR spectroscopies are performed to characterize polymers (PAEK, PAEK–COOH, and PAEK-*g*-PEG), as shown in Fig. S1 and S2,† respectively. Fig. S1a† show that proton signals at $\delta = 8.62$, 7.96 ppm were assigned to $H_1$, $H_{2,3,4}$ of DHPZ while those at $\delta = 7.84$, 7.69, 7.16, ppm were assigned to $H_{9,10}$, $H_8$ and $H_7$ of DFBP. In Fig. S1b† peaks at 12.06, 2.35, 2.01, 1.58 were assignable to protons $H_{15}$, $H_{12}$, $H_{13}$ and $H_{14}$. Notably, new peaks in Fig. S1c† were observed at 3.63 and 3.37 ppm in the PAEK-*g*-PEG spectrum due to the grafted PEG segments. Structures of these copolymers were further confirmed *via* FT-IR spectroscopy (Fig. S2†). Absorption bands at 1103 and 2928 $cm^{-1}$ were formed due to the respective stretching vibrations of –C–O–C– and $-CH_2$ in grafted PEG segments. As expected, polymers PAEK, PAEK–COOH, and PAEK-*g*-PEG were successfully synthesized.

## 3.2 Thermal characterization and morphologies of composite microporous membranes

Thermal stabilities of MPEs were investigated *via* TGA. The results are shown in Fig. 1a. TGA curves of composite membranes indicated a two-step weight loss process, except for the pure PAEK membrane (S0). The weight loss in the first step occurred at 175 °C, which was considered the loss of grafted PEG pendants. The weight loss in the second step occurred at 375 °C, which was considered the loss of the PAEK polymer backbone. However, $T_{5\%}$ of all membranes was higher than 220 °C. Therefore, the thermal stability of composite microporous polymer membranes can be used for the electrolyte membrane of supercapacitors.

Fig. 2 and S4† show the SEM images of composite microporous membranes and commercial separator. The number of pores and pore diameter on the surface increased and reached the maximum when the PAEK-*g*-PEG content was approximately 30 wt%. The PAEK-*g*-PEG content further increased and the pore distribution became sparse. This is because the hydrophilic segment of PEG interacts properly with isopropanol through hydrogen bonds. Hence, isopropanol was evenly dispersed in the membrane during the solvent–nonsolvent exchange and the pore distribution was uniform and dense. The interaction resulted in the retardation of the solvent–nonsolvent exchange in the composite membrane and increase of pore size. However, the accumulation of isopropanol mainly in the PEG phase decreased the pore distribution when the PAEK-*g*-PEG content was 40%. The creation of ion transport channels in microporous membranes was presented in this work. The hydrophilic PEG segment moved to the isopropanol-rich phase and remained on the resulting pore surface in the process of pore formation.[47,48] Therefore, this pore structure of composite microporous membranes was beneficial to the transport of lithium ions. The ionic conductivity of MPEs mainly depends on the liquid phase.[44] Therefore, the porosity of composite

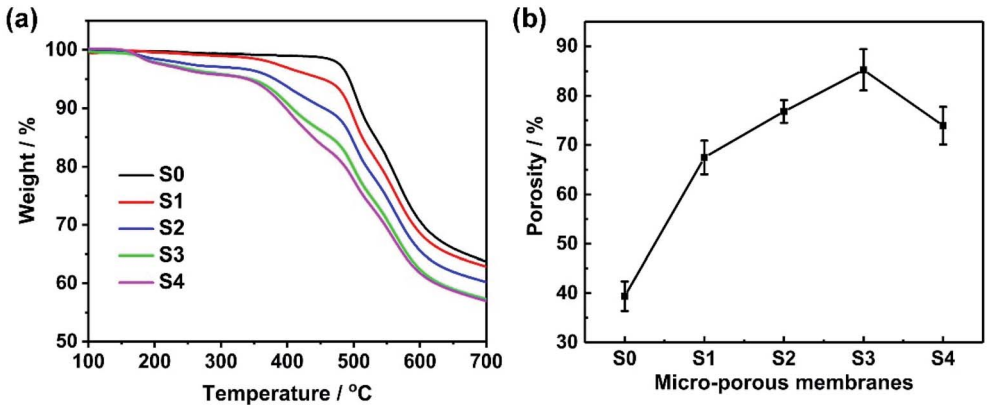


Fig. 1 (a) TGA curves and (b) porosities of microporous membranes (S0–S4).

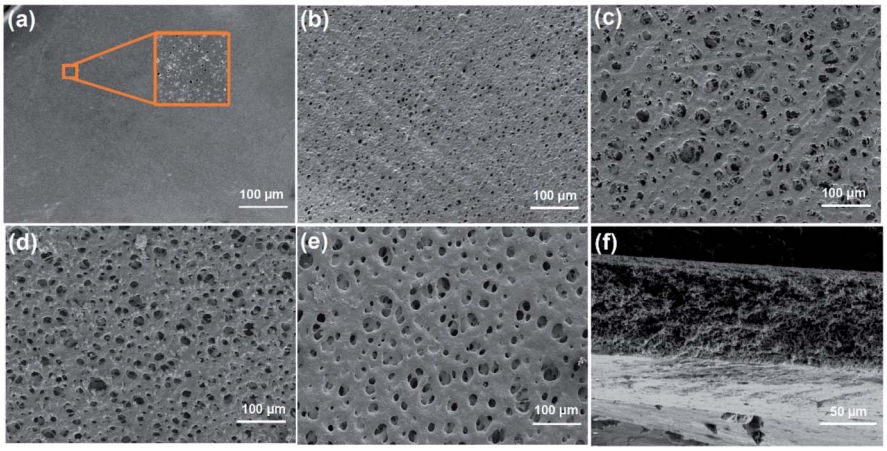


Fig. 2 Surface morphologies of the fabricated micro-porous membranes (a) S0, (b) S1, (c) S2, (d) S3, and (e) S4 and (f) cross-section image of S3.

microporous membranes is a significant factor, which was measured *via* the ethanol uptake test. The results are presented in Table 1 and Fig. 1b. The porosity of polymer membranes reach the maximum value (84.2%), which was significantly greater than that of the commercial separator (39.6%), when the ratio of PAEK to PAEK-*g*-PEG was 7 : 3. Furthermore, the result was consistent with SEM images (Fig. 2).

Morphologies and porosities of composite microporous membranes demonstrated that S3 is the most suitable electrolyte membrane for supercapacitors.

### 3.3 Aqueous electrolyte absorption and leakage rates of MPEs

Ion transport mainly occurs in the liquid phase of microporous polymer membranes. Therefore, absorption and leakage rates of the aqueous electrolyte directly influence the transport of ions. Absorption and leakage rates of the microporous electrolyte membrane S3 and the commercial separator are shown in Fig. 3a and b, respectively.

The liquid absorption of S3 first increased and then decreased when a certain amount of chitosan was added to the $LiClO_4$ aqueous electrolyte and the liquid absorption rate reached the maximum when the chitosan content was 2% because carboxylated chitosan contains a lot of amino ($-NH_2$), hydroxyl (–OH) and carboxyl groups (–COOH). Due to the presence of a large number of hydrophilic groups, it has a high degree of hydrophilicity, which helps to maintain a high moisture content in the polymer matrix, thus enhancing the ionic conductivity. However, the further increase in the concentration of chitosan in the liquid, the volume fraction of carboxylated chitosan increases more and the carboxylated chitosan in the porous membrane becomes the main component, while the water content is greatly reduced. In addition, the liquid absorption of the commercial separator immersed in the aqueous electrolyte containing 2% chitosan was not as high as that of any S3 membrane mainly due to the low porosity of the commercial separator. The electrolyte leakage rate of the microporous electrolyte membrane S3 and the commercial separator are illustrated in Fig. 3b. The introduction of chitosan reduced the electrolyte leakage. The high content of chitosan indicates the low electrolyte leakage for S3. The leakage rate of the commercial separator was significantly greater than that of S3 when the chitosan content was 2% likely due to the affinity of

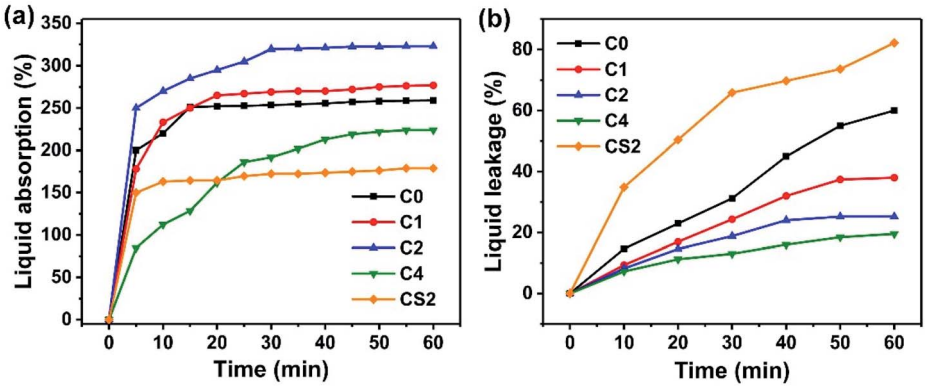


Fig. 3 Liquid electrolyte (a) absorption and (b) leakage rates of the microporous electrolyte membrane S3 formed using various chitosan concentrations and the commercial separator formed using 2% chitosan concentration.

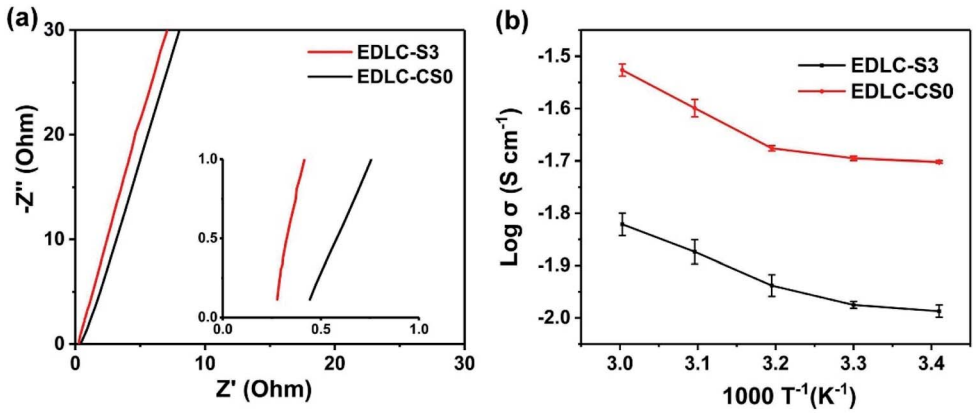


Fig. 4 (a) EIS Nyquist plot for the frequency range of 100 kHz to 1 Hz at 293 K. (b) Temperature dependence (293–333 K) of the ionic conductivity of the MPE S3 using 1 M $LiClO_4$ aqueous solution with 2% chitosan concentration and CS0 using 1 M $LiClO_4$ aqueous solution without chitosan.

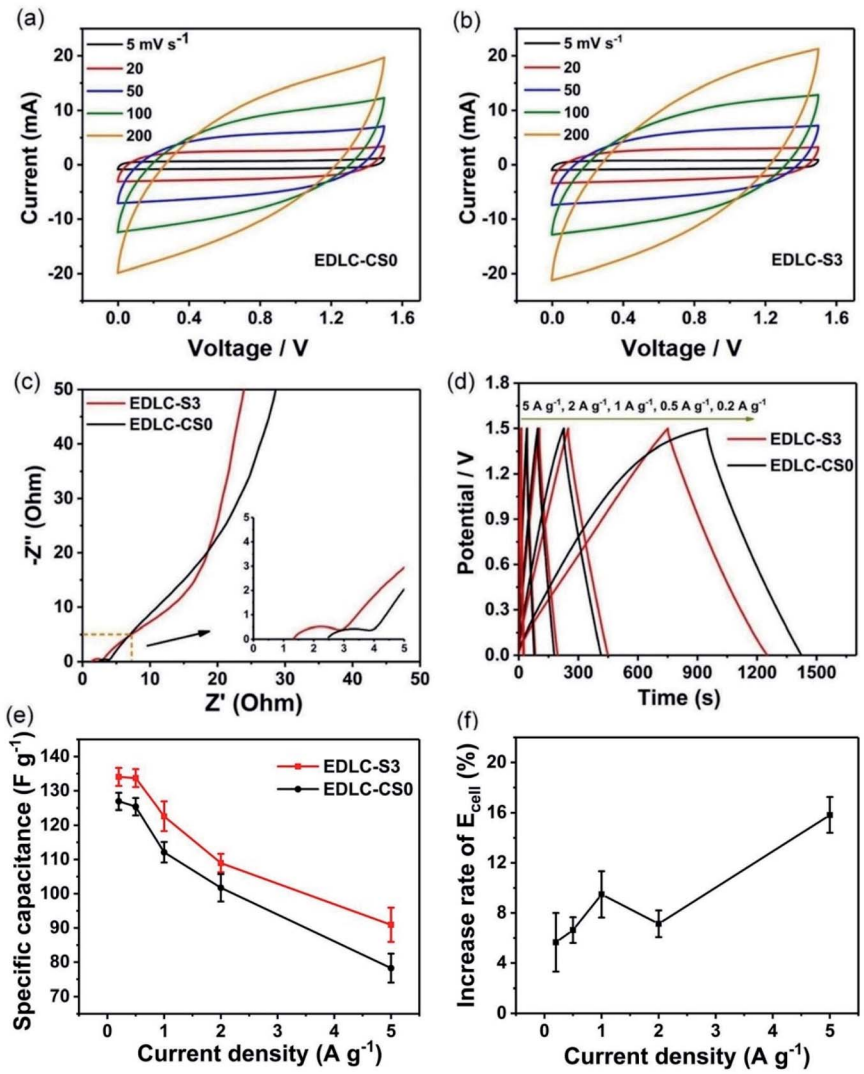


Fig. 5 CV curves of (a) EDLC-CS0 and (b) EDLC-S3 at different scan rates (5–200 mV $s^{-1}$). (c) EIS Nyquist plot for the frequency range of 0.01 Hz to 100 kHz. (d) GCD curves of EDLC-CS0 and EDLC-S3 at various current densities. (e) Specific capacitance and (f) increase rate of energy density for EDLC-CS0 and EDLC-S3 at different current densities.

PEO and chitosan.[36] In conclusion, the maximum positive effect of the chitosan content of 2% in the aqueous $LiClO_4$ electrolyte on absorption and leakage rates of microporous polymer membrane S3 is suitable for solid-state EDLCs. Therefore, we used the S3 membrane with 1 M $LiClO_4$ aqueous solution with 2% chitosan concentration for the following experiments.

### 3.4 Ionic conductivities of the polymer electrolyte S3 using the 1 M $LiClO_4$ aqueous solution with 2% chitosan concentration

Ionic conductivity, a key parameter for electrolyte applications,[19] was investigated at various temperatures (from 293 K to 333 K) for composite polymer electrolytes S3 and CS0. Fig. 4a and b present EIS Nyquist plot at 293 K and the temperature dependence of ionic conductivities in Arrhenius plots of CS0 and S3. The ionic conductivity of S3 and CS0 increased with increasing temperature. The thickness of S3 and commercial separator CS used in this test was approximately 105 and 92 μm, respectively. The results showed that the $Li^+$ ion transport ability of S3 is nearly two times higher at $2 \times 10^{-2}$ S $cm^{-1}$ at 293 K (as shown in Fig. 4a) and $2.98 \times 10^{-2}$ S $cm^{-2}$ at 333 K compared with the ionic conductivity of CS0 at $1.03 \times 10^{-2}$ S $cm^{-1}$ at 293 K. This finding exhibited that abundant pore structures allow the lithium ion to move freely while the affinity of the EO unit of the grafted PEG chain to $Li^+$ ions further facilitates the transport of lithium ions.[49,50] In addition, the ion transport of the composite microporous membrane is unhindered by the added carboxylated chitosan.

### 3.5 Electrochemical performance of EDLC with MPE S3 and activated carbon electrodes

Two activated carbon (AC) electrodes with the same weight as working electrodes were assembled with S3 in the two-electrode system. The commercial separator with the 1 mol $L^{-1}$ $LiClO_4$ electrolyte without chitosan was assembled in the same way for comparison, as shown in Scheme 2. The two devices were labeled EDLC-S3 and EDLC-CS0. First, cyclic voltammograms of EDLC-S3 and EDLC-CS0 were obtained from 0.0 V to 1.5 V. Fig. 5a and b show that shapes of CV curves of EDLC-S3 and EDLC-CS0 were similar due to the excellent ionic conductivity. Quasi-rectangular shapes at scan rates of 5 and 100 mV $s^{-1}$ indicated their ideal capacitive behavior and low contact resistance.[12]

Electrochemical impedance spectroscopy (EIS) is commonly used to investigate the charge transfer in electrode, ion transport through electrolyte, and ion diffusion at the interface of electrolyte/electrode. We performed EIS measurements with frequencies from 0.01 Hz to 100 kHz for EDLC-S3 and EDLC-CS0, as shown in Fig. 5c. Nyquist plots of EDLC-S3 and EDLC-CS0 display a similar pattern. A linear part can be observed in the low-frequency region and a semicircle can be observed in the high-frequency region. A vertical line parallel to the imaginary axis ($Z''$) was shown in the plots of both EDLC-S3 and EDLC-CS0 in the low-frequency region, thereby indicating the ideal capacitive behavior of EDLC-S3 and EDLC-CS0. Both EDLC-S3 and EDLC-CS0 showed semicircles at 1.53 and 1.35 Ω, respectively, in the high-frequency region, thereby indicating the slightly higher interface transfer resistance of S3 than CS0.[51,52]

The galvanostatic charge/discharge (GCD) curves for EDLC-S3 and EDLC-CS0 devices at various current densities (0.2–5 A $g^{-1}$) in Fig. 6d exhibited a typical triangular shape that corresponds to ideal EDLC properties. The small voltage drop at the beginning of the discharging step for both of EDLC-S3 and EDLC-CS0 was associated with the overall resistance of the system.[19,53] Notably, the discharge time of EDLC-S3 at 499 s was longer than that of EDLC-CS0 at 475 s under the same current density of 0.2 A $g^{-1}$ and $C_s$ values of EDLC-S3 and EDLC-CS0 were 134.38 and 126.92 F $g^{-1}$, respectively. Hence, supercapacitors using S3 can obtain more specific capacitance than those with $LiClO_4$ liquid electrolyte due to the same electrode materials of the two devices. $C_s$ values at various current densities for EDLC-S3 and EDLC-CS0 are listed in Table S2.† Under all current densities, $C_s$ values of EDLC-S3 were slightly higher than that of $LiClO_4$ liquid electrolyte. The difference between EDLC-S3 and EDLC-CS0 is clearly illustrated in Fig. 5e. The $C_s$ value decreased gradually with the increase of the current density due to the reduced ion diffusion into the electrode. Moreover, $E_{cell}$ values of EDLC-S3 were also slightly higher than that of CS0 at different current densities. The energy density of the supercapacitor using S3 was 15.82%

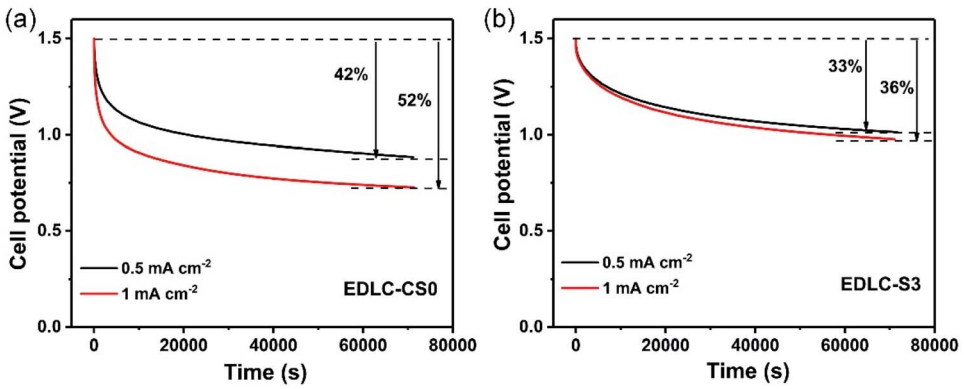


Fig. 6 Open-circuit potential decays of (a) conventional liquid supercapacitor EDLC-CS0 and (b) solid-state supercapacitor EDLC-S3.

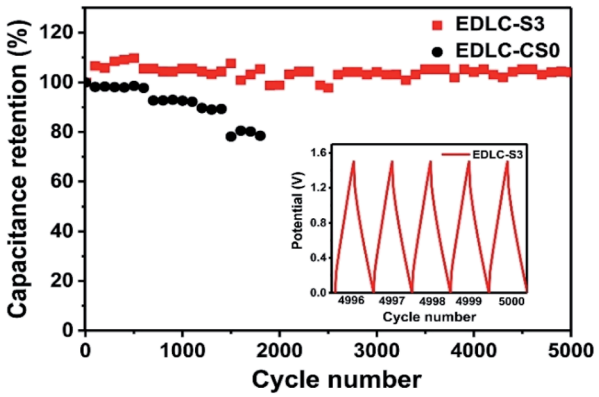


Fig. 7 Capacitance retention of the solid-state supercapacitor EDLC-S3 and the liquid supercapacitor EDLC-CS0 at a charging/discharging current density of 1 A $g^{-1}$.

higher than that of the supercapacitor using CS0 under a current density of 5 A $g^{-1}$ (Fig. 5f). These results can be attributed to the efficient ionic transport ability of S3.[19] $Li^+$ ions can diffuse into AC electrode pores more effectively, even at high current densities, due to the enhanced ionic transport ability of MPE S3 (Fig. 4), thereby enhancing $C_s$ and $E_{cell}$ values of supercapacitors.[54,55]

Apart from the specific capacitance, energy density, and ionic conductivity, the rapid self-discharge phenomenon also severely limits the application of supercapacitors. Self-discharge tests for S3 and CS0 were performed. Fig. 6a and b show the decay of open-circuit potential after charging at different current densities (0.5 and 1 mA $cm^{-2}$) for S3 and CS0, respectively. Compared with EDLC-CS0, EDLC-S3 displayed a lower self-discharge behavior of only 33% and 36% after charging current densities of 0.5 and 1 mA $cm^{-2}$, respectively, within 70 000 s. This finding is significantly better than that of conventional supercapacitors (42% and 52% after charging current densities of 0.5 and 1 mA $cm^{-2}$, respectively, within 70 000 s). Hence, S3 can restrain the self-discharge behavior of supercapacitors to a certain extent due to excellent electrical insulation characteristics of the electrolyte S3.[56,57]

The cycle stability of the EDLC-S3 device was also evaluated at a constant charging/discharging current density of 1 A $g^{-1}$, as shown in Fig. 7. The capacitance retention value of EDLC-S3 remained nearly constant in over 5000 cycles due to the enhanced liquid retention ability of EDLC-S3. Owing to the flow and leakage of the aqueous electrolyte, the specific capacitance of the liquid supercapacitor EDLC-CS0 began to decay after 600 cycle. Therefore, excellent electrochemical characteristics of the composite microporous membrane achieved in this study indicate its suitability for use in practical EDLCs.

## 4. Conclusion

We successfully developed a novel PAEK/PAEK-*g*-PEG microporous electrolyte S3, which was formed using carboxylated chitosan with a concentration of 2%. The novel MPE demonstrated several advantages, such as high electrolyte absorption capacity, high thermal stability, and excellent ionic conductivity ($2 \times 10^{-2}$ S $cm^{-1}$ at room temperature). Symmetric solid-state EDLC that combines microporous electrolyte S3 with activated carbon electrodes exhibited high electrochemical performance conductivity. The high specific capacitance of solid-state EDLC-S3 reached 134.38 F $g^{-1}$ with a potential window of 0–1.5 V and exhibited low internal resistance, improved cycling performance, and low self-discharge behavior. Thus, our study provides a promising and new direction for developing solid-state electrolytes in the field of solid-state electronics devices.

## Conflicts of interest

This authors declare no conflict of interest.

## Acknowledgements

The authors acknowledge the support from the National Key Research and Development Program (No. 2018YFB1107500), LiaoNing Revitalization Talents Program (No. XLYC1907144), the National Natural Science Foundation of China (No. 51503024), Dalian Youth Science and Technology Star Project Support Program (No. 2017RQ104).

## References

1 J. S. M. Lee, M. E. Briggs, C. C. Hu and A. I. Cooper, *Nano Energy*, 2018, **46**, 277–289.
2 J. Li, Y. Wang, W. Xu, Y. Wang, B. Zhang, S. Luo, X. Zhou, C. Zhang, X. Gu and C. Hu, *Nano Energy*, 2019, **57**, 379–387.
3 Q. Meng, K. Cai, Y. Chen and L. Chen, *Nano Energy*, 2017, **36**, 268–285.
4 N. L. W. Septiani, Y. V. Kaneti, K. B. Fathoni, J. Wang, Y. Ide, B. Yuliarto, Nugraha, H. K. Dipojono, A. K. Nanjundan, D. Golberg, Y. Bando and Y. Yamauchi, *Nano Energy*, 2020, **67**, 104270.
5 S. W. Zhang, B.-S. Yin, X. X. Liu, D. M. Gu, H. Gong and Z.-B. Wang, *Nano Energy*, 2019, **59**, 41–49.
6 Y. Zhang, J. He, Z. Gao and X. Li, *Nano Energy*, 2019, **65**, 41–49.
7 L. L. Zhang and X. S. Zhao, *Chem. Soc. Rev.*, 2009, **38**, 2520–2531.
8 Z. Yu, L. Tetard, L. Zhai and J. Thomas, *Energy Environ. Sci.*, 2015, **8**, 702–730.
9 Y. Gao, Y. S. Zhou, M. Qian, X. N. He, J. Redepenning, P. Goodman, H. M. Li, L. Jiang and Y. F. Lu, *Carbon*, 2013, **51**, 52–58.
10 F. Wang, X. Wu, X. Yuan, Z. Liu, Y. Zhang, L. Fu, Y. Zhu, Q. Zhou, Y. Wu and W. Huang, *Chem. Soc. Rev.*, 2017, **46**, 6816–6854.
11 A. Borenstein, O. Hanna, R. Attias, S. Luski, T. Brousse and D. Aurbach, *J. Mater. Chem. A*, 2017, **5**, 12653–12672.
12 R. Na, G. Huo, S. Zhang, P. Huo, Y. Du, J. Luan, K. Zhu and G. Wang, *J. Mater. Chem. A*, 2016, **4**, 18116–18127.
13 X. Zhang, X. Wang, L. Jiang, H. Wu, C. Wu and J. Su, *J. Power Sources*, 2012, **216**, 290–296.

14 C. M. Yang, Y. J. Kim, M. Endo, H. Kanoh, M. Yudasaka, S. Iijima and K. Kaneko, *J. Am. Chem. Soc.*, 2007, **129**, 20–21.
15 C. Wu, X. Wang, B. Ju, L. Jiang, H. Wu, Q. Zhao and L. Yi, *J. Power Sources*, 2013, **227**, 1–7.
16 C. Meng, C. Liu, L. Chen, C. Hu and S. Fan, *Nano Lett.*, 2010, **10**, 4025–4031.
17 H. Liao, H. Hong, H. Zhang and Z. Li, *J. Membr. Sci.*, 2016, **498**, 147–157.
18 D. Kalpana, N. G. Renganathan and S. Pitchumani, *J. Power Sources*, 2006, **157**, 621–623.
19 R. Na, Y. Liu, N. Lu, S. Zhang, F. Liu and G. Wang, *Chem. Eng. J.*, 2019, **374**, 738–747.
20 Y. Liu, T. Xiao, C. Bao, Y. Fu and X. Yang, *J. Membr. Sci.*, 2018, **563**, 298–308.
21 T. Xiao, P. Wang, X. Yang, X. Cai and J. Lu, *J. Membr. Sci.*, 2015, **489**, 160–174.
22 H. J. Zhu, W. Zhai, M. Yang, X.-m. Liu, Y. C. Chen, H. Yang and X. d. Shen, *RSC Adv.*, 2014, **4**, 25625–25632.
23 W. Zhai, H. j. Zhu, L. Wang, X. m. Liu and H. Yang, *Electrochim. Acta*, 2014, **133**, 623–630.
24 X. Zhang, L. Wang, J. Peng, P. Cao, X. Cai, J. Li and M. Zhai, *Adv. Mater. Interfaces*, 2015, **2**, 1500267.
25 J. Y. Song, Y. Y. Wang and C. C. Wan, *J. Power Sources*, 1999, **77**, 183–197.
26 F. Croce, F. Gerace, G. Dautzemberg, S. Passerini, G. B. Appetecchi and B. Scrosati, *Electrochim. Acta*, 1994, **39**, 2187–2194.
27 Y. Y. Lee and Y.-L. Liu, *Electrochim. Acta*, 2017, **258**, 1329–1335.
28 K. Tsunemi, H. Ohno and E. Tsuchida, *Electrochim. Acta*, 1983, **28**, 833–837.
29 T. P. Lodge, *Science*, 2008, **321**, 50–51.
30 V. K. Thakur, G. Ding, J. Ma, P. S. Lee and X. Lu, *Adv. Mater.*, 2012, **24**, 4071–4096.
31 C. Y. Tsai, K. J. Peng, C.-F. Wang and Y. L. Liu, *ACS Sustainable Chem. Eng.*, 2020, **8**, 2138–2146.
32 I. Shin, J. Nam, K. Lee, E. Kim and T. H. Kim, *Polym. J.*, 2018, **9**, 42.
33 T. Dong, J. Hu, M. Ueda, Y. Wu, X. Zhang and L. Wang, *J. Mater. Chem. A*, 2016, **4**, 2321–2331.
34 T. Hamada, S. Hasegawa, H. Fukasawa, S. i. Sawada, H. Koshikawa, A. Miyashita and Y. Maekawa, *J. Mater. Chem. A*, 2015, **3**, 20983–20991.
35 K. Miyatake, Y. Chikashige, E. Higuchi and M. Watanabe, *J. Am. Chem. Soc.*, 2007, **129**, 3879–3887.
36 K. Yuan, C. Liu, J. Han, G. Yu, J. Wang, H. Duan, Z. Wang and X. Jian, *RSC Adv.*, 2016, **6**, 12009–12020.
37 K. Yuan, C. Liu, L. Zong, G. Yu, S. Cheng, J. Wang, Z. Weng and X. Jian, *ACS Appl. Mater. Interfaces*, 2017, **9**, 13201–13212.
38 L. Zong, C. Liu, Y. Guo, J. Wang and X. Jian, *RSC Adv.*, 2015, **5**, 77027–77036.
39 L. Zong, C. Liu, R. Liu, J. Wang and X. Jian, *Polym. Bull.*, 2014, **71**, 2641–2660.
40 C. W. Huang, C.-A. Wu, S.-S. Hou, P. L. Kuo, C. T. Hsieh and H. Teng, *Adv. Funct. Mater.*, 2012, **22**, 4677–4685.
41 K. Prabakaran, S. Mohanty and S. K. Nayak, *RSC Adv.*, 2015, **5**, 40491–40504.
42 Q. Sun, J. Wang, L. He, Y. Song and X. Jian, *J. Appl. Polym. Sci.*, 2007, **104**, 1744–1753.
43 Y. Du, K. Zhu, Y. Fang, S. Zhang, X. Zhang, Y. Lu, Y. Yang, Y. Song and G. Wang, *RSC Adv.*, 2015, **5**, 48311–48322.
44 X. Wang, C. Gong, D. He, Z. Xue, C. Chen, Y. Liao and X. Xie, *J. Membr. Sci.*, 2014, **454**, 298–304.
45 R. Na, C. W. Su, Y. H. Su, Y. C. Chen, Y. M. Chen, G. Wang and H. Teng, *J. Mater. Chem. A*, 2017, **5**, 19703–19713.
46 F. Hu, T. Zhang, J. Wang, S. Li, C. Liu, C. Song, W. Shao, S. Liu and X. Jian, *Nano Energy*, 2020, **74**, 104789.
47 M. M. Perez-Madrigal, F. Estrany, E. Armelin, D. Diaz Diaz and C. Aleman, *J. Mater. Chem. A*, 2016, **4**, 1792–1805.
48 B. Cheng, B. Pei, Z. Wang and Q. Hu, *RSC Adv.*, 2017, **7**, 42036–42046.
49 C. Y. Tsai, K. J. Peng, C. F. Wang and Y. L. Liu, *ACS Sustainable Chem. Eng.*, 2020, **8**, 2138–2146.
50 W. Wang, S. Guan, M. Li, J. Zheng and C. Xu, *Org. Electron.*, 2018, **56**, 268–275.
51 Y. Sun, W. Zhang, D. Li, L. Gao, C. Hou, Y. Zhang and Y. Liu, *Electrochim. Acta*, 2015, **178**, 823–828.
52 G. Guo, Y. Sun, Q. Fu, Y. Ma, Y. Zhou, Z. Xiong and Y. Liu, *Int. J. Hydrogen Energy*, 2019, **44**, 6103–6115.
53 M. M. Perez-Madrigal, F. Estrany, E. Armelin, D. Diaz Diaz and C. Aleman, *J. Mater. Chem. A*, 2016, **4**, 1792–1805.
54 H. Huang, X. Zeng, W. Li, H. Wang, Q. Wang and Y. Yang, *J. Mater. Chem. A*, 2014, **2**, 16516–16522.
55 Y. E. Miao, W. Fan, D. Chen and T. Liu, *ACS Appl. Mater. Interfaces*, 2013, **5**, 4423–4428.
56 Z. Wang, Z. Xu, H. Huang, X. Chu, Y. Xie, D. Xiong, C. Yan, H. Zhao, H. Zhang and W. Yang, *ACS Nano*, 2020, **14**, 4916–4924.
57 Z. Wang, X. Chu, Z. Xu, H. Su, C. Yan, F. Liu, B. Gu, H. Huang, D. Xiong, H. Zhang, W. Deng, H. Zhang and W. Yang, *J. Mater. Chem. A*, 2019, **7**, 8633–8640.